SSC22-P4-22

Thermal Modeling of FEMTA Micropropulsion System for CubeSat Attitude Control

Florian Alexander Hoeft
Karlsruhe Institute of Technology
Kaiserstraße 12, 76131 Karlsruhe, Germany
florian.hoeft@student.kit.edu

Steven Pugia, Alina Alexeenko
Purdue University School of Aeronautics and Astronautics
701 W. Stadium Ave., West Lafayette, IN
spugia@purdue.edu

ABSTRACT

Nano and pico-class satellite platforms such as 1U CubeSats, PocketQubes, and ThinSats introduce unique power and volume constraints on propulsion systems. The Film-Evaporation MEMS Tunable Array (FEMTA) microthruster is one compact, low-power technology that is well suited for these applications. FEMTA thrusters are microfabricated on 1 cm x 1 cm x 1 mm silicon and glass chips. Each chip contains an array of micrometer-scale capillaries which are electrically heated to vaporize the liquid propellant and generate controlled thrust. Sixth generation FEMTA devices have been demonstrated to produce greater than 300 microNewton of thrust per 1 Watt of electrical power at 90 seconds specific impulse. Liquid ultra-pure deionized water is used as a dense, safe, and abundantly available propellant source. A complete FEMTA six degree-of-freedom propulsion system including zero-gravity propellant management is being developed at Purdue University in preparation for a future orbital flight demonstration. It is suspected that the performance and long-term reliability of FEMTA will be sensitive to temperature fluctuations within this propulsion system while in orbit. Specifically, a reduction in propellant temperature may result in ice generation within the FEMTA chips and an increase in propellant temperature will reduce total DeltaV through higher quiescent propellant loss. We present an investigation of FEMTA propulsion system thermal response in Low Earth Orbit (LEO). A generalizable analysis process was developed for LEO CubeSat missions using finite element models in ANSYS. This analysis process was applied to a preliminary CubeSat mission design to investigate FEMTA propulsion system transient-thermal behavior. Model accuracy and recommendations for future improvements to the process are discussed.

INTRODUCTION

The miniaturizing of satellites has created new demand for exceptionally compact, power efficient, and precise propulsion technologies for attitude control and maneuvering. Traditional propulsion technologies have been adapted for the nanosatellite platform including chemical bipropellant and monopropellant, cold and warm gas, and resistojet thrusters. However, these approaches can require large portions of a nanosatellites mass or power budget while typically offering impulse bit sizes no less than 100 µN s.

One potential alternative being developed at Purdue University is the Film-Evaporation MEMS Tunable Array (FEMTA) microthruster. FEMTA can produce more than 300 µN of highly tunable thrust per 1 W of electrical power by inducing controlled evaporation of liquid ultra-pure deionized water (UPW) in an array of micrometer-scale silicon capillaries (figure 1).[1,2] While not generating thrust, capillary forces prevent the liquid water from exiting the microcapillaries. Thrust output is proportional to electrical power input and can be throttled down to the nanoNewton range. Additionally, since no mechanical actuation is required to operate the device and since energy deposition is highly concentrated at the micrometer scale, FEMTA minimum impulse bit size is much smaller than traditional techniques. Satellite controllability is further enhanced by the fact that the quantity and orientation of these microcapillaries may be customized on each chip to suite the unique requirements of a satellite.

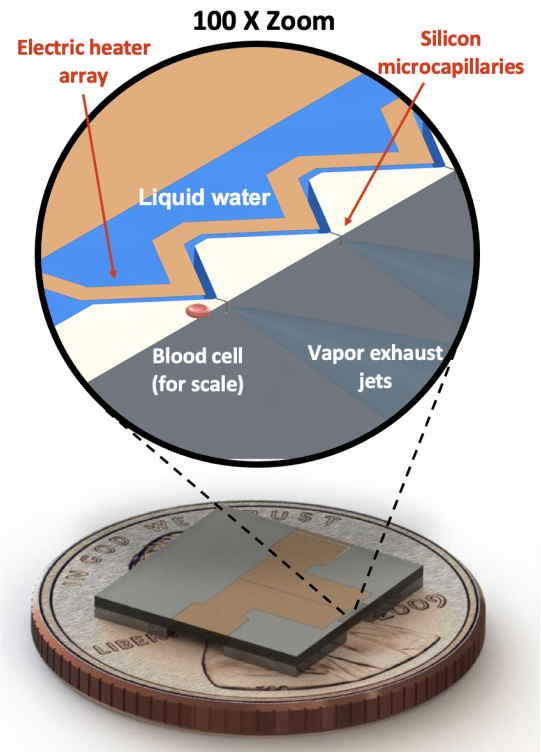

Figure 1: FEMTA thruster chip with US penny for scale and diagram of the microcapillary array

The FEMTA microthrusters employ a novel means of managing propellant in micro-gravity which is similarly compact and power efficient. A single propellant volume is separated by a thin, flexible diaphragm with liquid UPW on one side and a small amount of a high vapor pressure fluid on the other (figure 2). As propellant is consumed, the high vapor pressure fluid evaporates to back-fill the volume. This technique is especially well suited for FEMTA since it's propulsive performance does not depend on liquid propellant pressure assuming that pressure is between approximately 20 kPa and 80 kPa.[1] No moving parts or active regulation systems are required thus resulting in large propellant mass fractions for the system as a whole.

FEMTA introduces some temperature constraints which need to be considered when designing a complete propulsion system. Firstly, propellant feed pressure must be between 20 kPa and 80 kPa to ensure reliable operation of the thruster chips. Therefore, pressurant liquid temperature must be maintained such that its vapor pressure remains within these limits. Another important factor is quiescent evaporation in the FEMTA at the liquid-vapor interfaces within the microcapillaries. Even when no power is applied to the heating elements, a small amount of water vapor is lost due to evaporation. At room temperature conditions, this quiescent evaporation generates a nanoNewton level background thrust. However, as propellant feed temperature increases, the magnitude of this background thrust increases and the DeltaV of the propulsion system decreases. Additionally, since the evaporation causes a quiescent cooling at the fluid interfaces, the temperature of the propellant entering the chips cannot drop below a certain threshold or otherwise ice formation may occur.[3] Combining these constraints, we arrive at a final set of temperature requirements for the FEMTA propulsion system: the temperature of all fluids within the propulsion system must be no less than 15 °C and no greater than 30 °C.

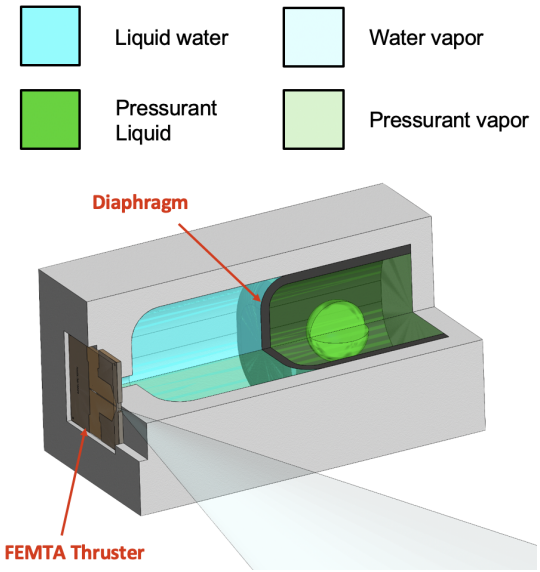

Figure 2: FEMTA zero-gravity propellant management system theory of operation

The objective of this research is to develop a generalized transient-thermal model and solution procedure for analyzing CubeSats operating in LEO and to use this model to perform a preliminary evaluation of the current FEMTA propulsion system design. The results of this preliminary study will be used to inform future thermal management system designs for the FEMTA propulsion system.

SATELLITE DESIGN

A preliminary CubeSat design including a FEMTA micropropulsion system was created for the purpose of developing this analysis procedure. The satellite has a 2U form factor and includes an imag-

ing system as its primary payload. The FEMTA propulsion system, shown in figure 3, consists of a central vapor-pressure driven propellant tank which supplies liquid UPW to each of the twelve FEMTA thruster chips through 0.125 inch diameter tubing and microfluidic fittings. Each chip is housed within nodes which are distributed throughout the satellite.

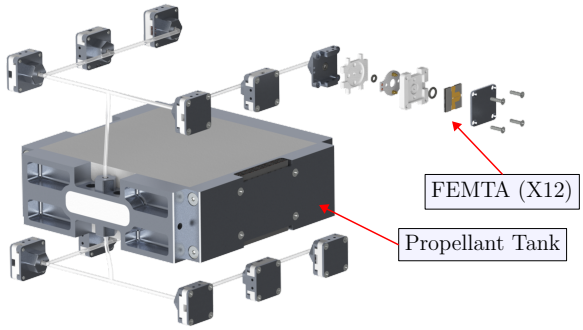

Figure 3: Preliminary FEMTA propulsion system design

The thruster nodes are integrated into the structure of the satellite frame to save space while allowing the chips to be placed in the optimal thrusting orientation for six DOF maneuvering (figure 4). The propellant tank, which has a 10 cm x 10 cm x 5 cm form factor, slides onto the rails which join the two groups of thruster nodes.

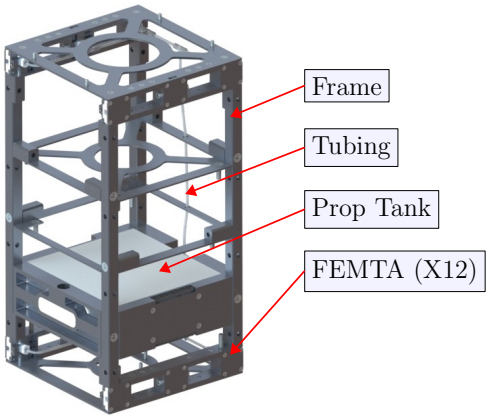

Figure 4: Structural frame and propulsion system for the CubeSat design

An exploded view of the entire satellite design is shown in figure 5. All off-the-shelf components were chosen from GOMSpace for compatibility. The electrical power system consists of one BPX battery pack containing eight 2600 mA h lithium ion cells and two heating elements for temperature regulation. Power is generated by eight P110 solar cells which each have a peak power output of approximately 2.3 W in LEO. Command and data handling is performed by the NanoMind A3200 which also includes a three-axis gyroscope and magnetometer for attitude sensing. Guidance and navigation is further enhanced by the OEM719 GPS transceiver and Tallysman TW1320 antenna. Data can be up-linked or down-linked through the ANT430 UHF antenna and AX100 half-duplex RF transceiver. Lastly, the GOMSpace C1U 3-megapixel camera with a 70 mm lens is used as an Earth imaging payload sensor.

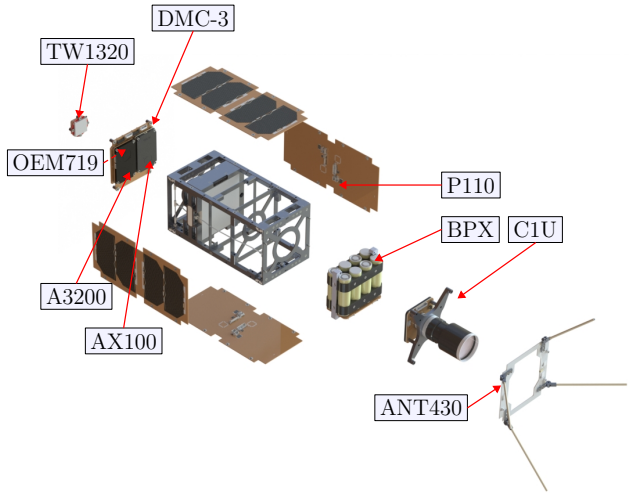

Figure 5: Exploded view

METHODOLOGY

ORBIT SELECTION

An orbit is uniquely defined by the six classical orbital elements (COEs), namely the semi-major axis (a), eccentricity (e), orbital inclination (i), right-ascension of the ascending node /RAAN (Ω), argument of perigee (ω), and true anomaly (ν).[4] The goal of this section is to select a realistic orbit appropriate for the preliminary CubeSat design and underlying operation. This orbit will later define the main boundary conditions for the thermal analysis process.

As of 2021, more than 1800 CubeSats have been launched and roughly 60 % have achieved their primary mission goal.[5,6] The *Nanosats Database* and *Gunter's Space Page* provided the necessary data to filter those CubeSats considering general restrictions on size, mission status and the scientific objective.[6,7] For the 60 CubeSats matching the restrictions, the COEs were gathered using active tracking websites, namely *CelesTrak* and *NY2O*, who receive their data from the US Air Force Space Command

(AFSPC) Space Surveillance Network.[8,9] Because a future FEMTA spaceflight mission is being developed in collaboration with the Air Force Office of Scientific Research (AFOSR) University Nanosatellite Program (UNP), an orbit likely to be launched at Air Force Western Test Range (AFWTR) was selected. It's orbital elements are displayed in table 1. It is an almost circular low Earth orbit. For future applications of this analysis process, the orbit will most likely be defined by the launch provider.

Table 1: Orbit selection

Name	a (km)	e	i (°)	Ω (°)	ω (°)
AFWTR	6936.84	0.00670	97.58	9.80	90

DYNAMIC MODEL

Three reference frames are applied to model the position of the CubeSat and its parts relative to inertial space, as shown in figure 6.[4,10–12]

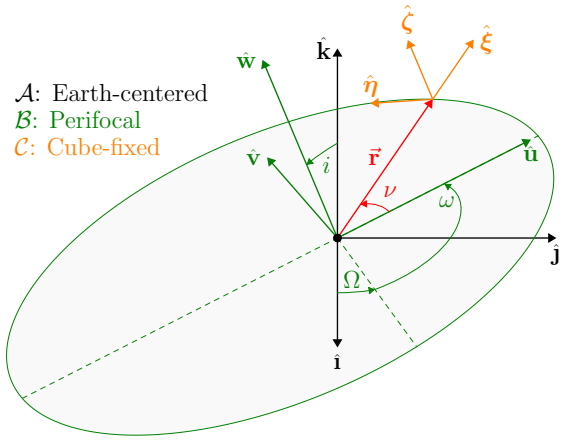

Figure 6: Applied coordinate systems

First, the cartesian Earth-centered equatorial reference frame is used as the inertial frame. It is denoted by the subscript $\mathcal{A}$ and described by its three unitary vectors [$\hat{\mathbf{i}}$, $\hat{\mathbf{j}}$, $\hat{\mathbf{k}}$]. Where $\hat{\mathbf{i}}$ points to the vernal equinox, $\hat{\mathbf{k}}$ denotes the Earth's axis of rotation and $\hat{\mathbf{j}}$ completes the equatorial plane and subsequently the right-handed coordinate system. The precession of Earth's rotational axis, as well as the resulting shift in the position of the vernal equinox, are ignored. The assumed reference frame is regarded as inertial and its position is fixed with respect to space and time.[4]

The CubeSat's orbit is approximated to be Keplerian and the perifocal coordinate system is used to describe the orientation and shape of the elliptical orbit. It is denoted by the subscript $\mathcal{B}$ and described by its three unitary vectors [$\hat{\mathbf{u}}$, $\hat{\mathbf{v}}$, $\hat{\mathbf{w}}$]. Where $\hat{\mathbf{u}}$ points to the periapsis, $\hat{\mathbf{w}}$ denotes the angular rotation vector and $\hat{\mathbf{v}}$ completes the elliptical plane.

Third, a cube-fixed reference frame is proposed to model its shape and any objects relative to it. It is non-inertial, denoted by the subscript $\mathcal{C}$, and described by its three unitary vectors [$\hat{\boldsymbol{\xi}}$, $\hat{\boldsymbol{\eta}}$, $\hat{\boldsymbol{\zeta}}$]. Where $\hat{\boldsymbol{\xi}}$, $\hat{\boldsymbol{\eta}}$, and $\hat{\boldsymbol{\zeta}}$ coincide with three edges of the cube.

Now, any arbitrary position vector in the perifocal reference frame:

$$\mathbf{r}_{\mathcal{B}} = \begin{bmatrix} r_1 \\ r_2 \\ r_3 \end{bmatrix} = r_1\hat{\mathbf{u}} + r_2\hat{\mathbf{v}} + r_3\hat{\mathbf{w}} \tag{1}$$

can be expressed in the Earth centered reference frame by applying a 3-1-3 Euler sequence:[13]

$$\mathbf{r}_{\mathcal{A}} = [\mathcal{R}_{\mathcal{B}\to\mathcal{A}}]\mathbf{r}_{\mathcal{B}} \tag{2}$$

Where $[R_{\mathcal{B}\to\mathcal{A}}]$ denotes the transformation into the inertial reference frame:

$$[\mathcal{R}_{\mathcal{B}\to\mathcal{A}}] = [\mathcal{R}_3(\Omega)][\mathcal{R}_1(i)][\mathcal{R}_3(\omega)] \tag{3}$$

In accordance with figure 6, the RAAN (Ω), argument of perigee (ω) and orbital inclination (i) form the three Euler Angles respectively:

$$[\mathcal{R}_3(\Omega)] = \begin{pmatrix} cos(\Omega) & -sin(\Omega) & 0 \\ sin(\Omega) & cos(\Omega) & 0 \\ 0 & 0 & 1 \end{pmatrix} \tag{4a}$$

$$[\mathcal{R}_1(i)] = \begin{pmatrix} 1 & 0 & 0 \\ 0 & cos(i) & -sin(i) \\ 0 & sin(i) & cos(i) \end{pmatrix} \tag{4b}$$

$$[\mathcal{R}_3(\omega)] = \begin{pmatrix} cos(\omega) & -sin(\omega) & 0 \\ sin(\omega) & cos(\omega) & 0 \\ 0 & 0 & 1 \end{pmatrix} \tag{4c}$$

The position of the CubeSat in the perifocal reference frame is obtained by introducing the mean anomaly ν:[10]

$$\mathbf{r}_{\mathcal{B}} = r(\nu)\begin{bmatrix} cos(\nu) \\ sin(\nu) \\ 0 \end{bmatrix} = \frac{a(1-e^2)}{1+e\,cos(\nu)}\begin{bmatrix} cos(\nu) \\ sin(\nu) \\ 0 \end{bmatrix} \tag{5}$$

For small eccentricities, the true anomaly may be approximated by the so-called Equation of the Center:[10]

$$\nu = M + \left(2e - \frac{1}{4}e^3\right)sin(M) + \frac{5}{4}e^2 sin(2M) + \frac{13}{12}e^3 sin(3M) \tag{6}$$

With M denoting the mean anomaly, which is linear in time (t):

$$M = 2\pi \left(\frac{t}{T} \right) \tag{7}$$

The orbital period T is defined through the semi-major axis and the standard gravitational parameter of earth (μ),[4] who's value is referenced in NASA's Earth Fact Sheet[14] as $\mu = 398\,600 \times 10^9\ \mathrm{m^3 s^{-2}}$:

$$T = 2\pi \sqrt{\frac{a^3}{\mu}} \tag{8}$$

Consequently, the position of the CubeSat ($\mathbf{r}$), as a function of time, in the inertial frame $\mathcal{A}$ can be defined uniquely through the six COEs:

$$\mathbf{r}_{\mathcal{A}}(a, e, i, \Omega, \omega, \nu) = [\mathcal{R}_{\mathcal{B}\to\mathcal{A}}]\mathbf{r}_{\mathcal{B}} \tag{9}$$

Modeling the attitude is done via the cube-fixed reference frame $\mathcal{C}$, as shown in figure 7. As the name suggests, its three unitary vectors coincide with the edges of the CubeSat. The CubeSat's six sides with their respective normal vectors are used to describe it's attitude.[12]

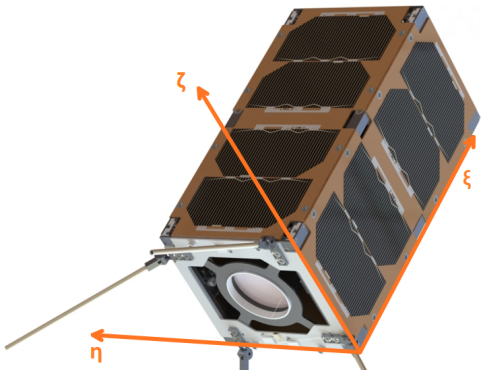

Figure 7: The cube-fixed reference frame

Following the same manner as in the position model, any vector in the cube-fixed reference frame $\mathcal{C}$ can be transformed into the perifocal frame $\mathcal{B}$ by applying a transformation matrix:

$$\mathbf{r}_{\mathcal{B}} = [\mathcal{R}_{\mathcal{C}\to\mathcal{B}}]\mathbf{r}_{\mathcal{C}} \tag{10}$$

, where the matrix $[\mathcal{R}_{\mathcal{C}\to\mathcal{B}}]$ can describe any rotation as a function of position and time. Subsequently,one is able to describe any vector in frame $\mathcal{C}$ with inertial coordinates in frame $\mathcal{A}$:

$$\begin{aligned} \mathbf{r}_{\mathcal{A}} &= [\mathcal{R}_{\mathcal{B}\to\mathcal{A}}][\mathcal{R}_{\mathcal{C}\to\mathcal{B}}]\mathbf{r}_{\mathcal{C}} \\ &= [\mathcal{R}_{tot}]\mathbf{r}_{\mathcal{C}} \end{aligned} \tag{11}$$

Thus, each face $\mathbf{n}_k$ ($k = 1...6$) in frame $\mathcal{C}$ may be transformed into frame $\mathcal{A}$. Their orientation in frame $\mathcal{C}$ at any point in time t is:

$$\mathbf{n}_{1_\mathcal{C}}(t) = \begin{bmatrix} 1 & 0 & 0 \end{bmatrix}^\intercal \tag{12a}$$
$$\mathbf{n}_{2_\mathcal{C}}(t) = \begin{bmatrix} -1 & 0 & 0 \end{bmatrix}^\intercal \tag{12b}$$
$$\mathbf{n}_{3_\mathcal{C}}(t) = \begin{bmatrix} 0 & 1 & 0 \end{bmatrix}^\intercal \tag{12c}$$
$$\mathbf{n}_{4_\mathcal{C}}(t) = \begin{bmatrix} 0 & -1 & 0 \end{bmatrix}^\intercal \tag{12d}$$
$$\mathbf{n}_{5_\mathcal{C}}(t) = \begin{bmatrix} 0 & 0 & 1 \end{bmatrix}^\intercal \tag{12e}$$
$$\mathbf{n}_{6_\mathcal{C}}(t) = \begin{bmatrix} 0 & 0 & -1 \end{bmatrix}^\intercal \tag{12f}$$

Now, a specific attitude behavior has to be defined in order to perform the transformation. In this analysis, a nadir pointing scheme is applied to accomodate the proposed Earth observation and imaging mission, as shown in figure 8.

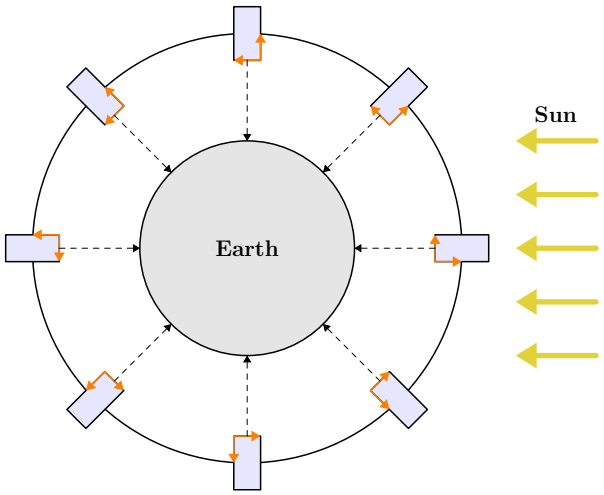

Figure 8: Nadir pointing scheme

To maintain the nadir pointing, the CubeSat has to rotate around the $\hat{\mathbf{w}}$ direction with the same angle as the true anomaly ν.[12]

$$[\mathcal{R}_{nadir}] = \begin{bmatrix} cos(\nu) & -sin(\nu) & 0 \\ sin(\nu) & cos(\nu) & 0 \\ 0 & 0 & 1 \end{bmatrix} \tag{13}$$

Since a strict nadir pointing scheme is not only unnecessarily restricting the satellite's field of view, but would also be obtainable using passive attitude control systems, a sweeping motion caused by the rotation around the satellite's velocity vector is applied. Figure 9 displays the increased field of view, depending on the angle κ. Shown is a 2U CubeSat orbiting earth at height h.

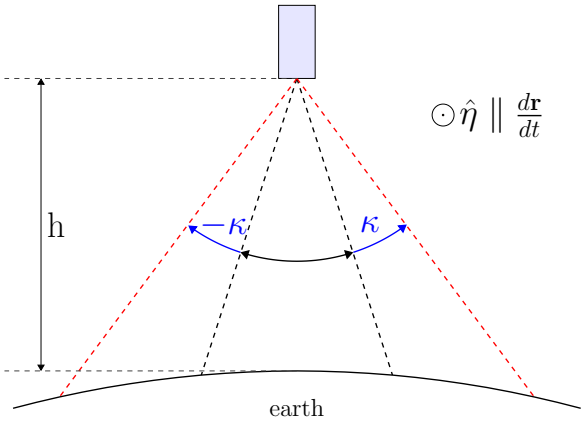

Figure 9: 2D field of view for the nadir pointing satellite

The rotation is described through:

$$[\mathcal{R}_{sweep}] = \begin{bmatrix} cos(\kappa) & 0 & sin(\kappa) \\ 0 & 1 & 0 \\ -sin(\kappa) & 0 & cos(\kappa) \end{bmatrix} \tag{14}$$

Where κ approximates a square wave:

$$\kappa = A_{sw} \cdot \frac{sin\left(\frac{2\cdot\pi\cdot n_{sw}\cdot t}{T}\right)}{\sqrt{sin\left(\frac{2\cdot\pi\cdot n_{sw}\cdot t}{T}\right)^2 + \varepsilon^2}} \tag{15}$$

Hereby defined with the following parameters: $A_{sw} = 10\,^\circ$, $n_{sw} = 6$ and $\varepsilon = 0.03$. Thus, the transformation and subsequently the attitude are fully defined:

$$[\mathcal{R}_{\mathcal{C}\to\mathcal{B}}] = [\mathcal{R}_{nad}][\mathcal{R}_{sweep}] \tag{16}$$

Finally, the orientation of all six sides of the CubeSat ($k = 1...6$) in the inertial frame of reference $\mathcal{A}$ is:

$$\begin{aligned} \mathbf{n}_{k_\mathcal{A}} &= [\mathcal{R}_{\mathcal{B}\to\mathcal{A}}][\mathcal{R}_{\mathcal{C}\to\mathcal{B}}]\mathbf{n}_{k_\mathcal{C}} \\ &= [\mathcal{R}_{\mathcal{B}\to\mathcal{A}}][\mathcal{R}_{nadir}][\mathcal{R}_{sweep}]\mathbf{n}_{k_\mathcal{C}} \end{aligned} \tag{17}$$

With that, a position and attitude model based on the orbits COEs is defined and may further be used to derive incident radiation.

RADIATION MODEL

In this section, a geometric approach to model the incident radiation on a CubeSat of arbitrary size is outlined using the above derived orbital model. Direct solar, albedo, and earth-infrared radiation are considered.

The sun is the source of virtually all the heat input to the solar system. With a total power output of roughly 3.856×10^{26} W, it dominates the solar space environment.[15] Within the span of this analysis, the sun is modeled as moving in regular motion with constant angular velocity relative to Earth, as shown in figure 10.[16]

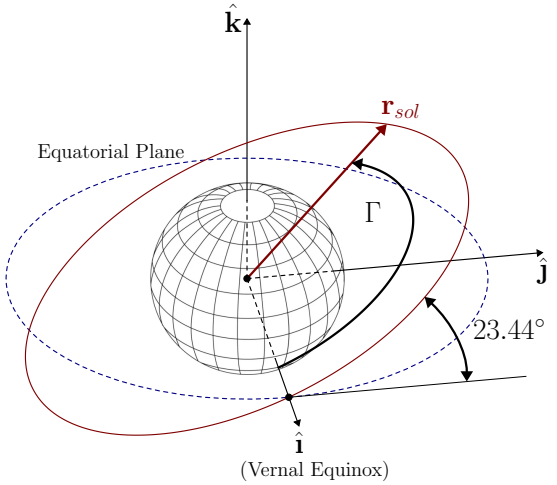

Figure 10: Solar position relative to Earth's equatorial plane

Its position in the elliptic plane is simply defined by:

$$\mathbf{r}_{sol} = r_{sol} \begin{bmatrix} cos(\Gamma) \\ sin(\Gamma) \\ 0 \end{bmatrix} \tag{18}$$

, where r_{sol} denotes 1AU and is set fixed to $r_{sol} = 1.495\,978\,707 \times 10^{11}$ m.[14] Its position over time is defined through the *Ecliptic True Solar Longitude* Γ, hereby defined as:

$$\Gamma = \frac{2\pi}{365.25\,\mathrm{d}}\, t + \Gamma_0 \tag{19}$$

, with Γ_0 simply denoting the initial position of the sun. It is transformed into the reference frame $\mathcal{A}$ by rotation about the $\hat{\mathbf{i}}$ direction, with the obliquity γ_{ecl}:[16]

$$\mathbf{r}_{sol_\mathcal{A}} = [\mathcal{R}_1(\gamma_{ecl})]\mathbf{r}_{sol} \tag{20}$$

$$[\mathcal{R}_1(\gamma_{ecl})] = \begin{bmatrix} 1 & 0 & 0 \\ 0 & cos(\gamma_{ecl}) & -sin(\gamma_{ecl}) \\ 0 & sin(\gamma_{ecl}) & cos(\gamma_{ecl}) \end{bmatrix} \tag{21}$$

, where $\gamma_{ecl} = 23.44\,°$. Note that the sun only rotates around this orbit once per year.

The sun's main characteristic relevant to thermal control is the total heat flux reaching Earth's atmosphere. At a distance of 1AU the solar constant G_s has an average value of $G_s = 1361\,\mathrm{W/m^2}$ and is assumed constant.[17] The total incident solar radiation on each face of the CubeSat $\mathbf{n}_{k_\mathcal{A}}$ $(k = 1...6)$ is:[18]

$$q_{k,solar} = G_s V F_{k\to s} \Lambda_{eclipse} \tag{22}$$

, where $VF_{k\to s} \in [0, 1]$ denotes the view factor between each face and the sun respectively:

$$VF_{k\to s} = \left(\frac{\mathbf{n}_{k_\mathcal{A}} \cdot \mathbf{r}_{sol_\mathcal{A}}}{\|\mathbf{n}_{k_\mathcal{A}}\| \, \|\mathbf{r}_{sol_\mathcal{A}}\|} \right) \Lambda_{VF_{k\to s}} \tag{23}$$

Since negative solar flux is not possible, the function $\Lambda_{VF_{k\to s}}$ is introduced:

$$\Lambda_{VF_{k\to s}} = \begin{cases} 1 & , (\mathbf{n}_{k_\mathcal{A}} \cdot \mathbf{r}_{sol_\mathcal{A}}) \geq 0 \\ 0 & , (\mathbf{n}_{k_\mathcal{A}} \cdot \mathbf{r}_{sol_\mathcal{A}}) < 0 \end{cases} \tag{24}$$

The function $\Lambda_{eclipse}$ ensures that the spacecraft has to be in the sun's line of sight to receive any direct solar radiation (figure 11).[18]

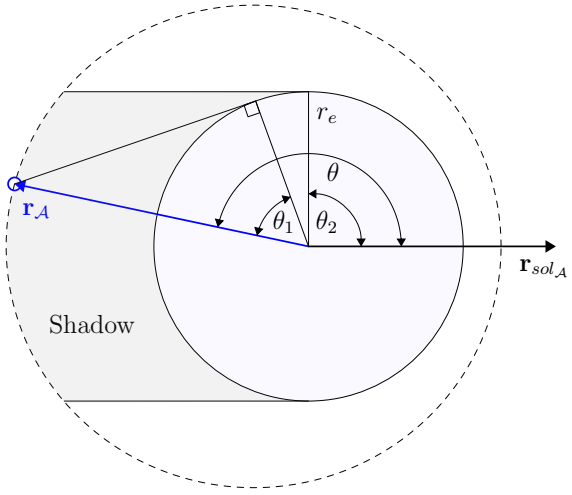

Figure 11: Earth casting a shadow

Earth is modeled as a perfect sphere of radius $r_e = 6.378\,137 \times 10^6\,\mathrm{m}$, casting a cylindrical shadow.[14] Sun rays originate from the point defined through the solar vector. Based on figure 11, this yields the following condition:[12]

$$\Lambda_{eclipse} = \begin{cases} 0 & , \theta_1 + \theta_2 \leq \theta \\ 1 & , \theta_1 + \theta_2 > \theta \end{cases} \tag{25}$$

Where θ_1 is defined as:

$$\theta_1 = \arccos\left(\frac{r_e}{\|\mathbf{r}_\mathcal{A}\|} \right) \tag{26}$$

And analogously θ_2 is:

$$\theta_2 = \arccos\left(\frac{r_e}{\|\mathbf{r}_{sol_\mathcal{A}}\|} \right) \approx \frac{\pi}{2} \tag{27}$$

Lastly, the angle θ is defined as the angle between the position vector of the satellite and the sun:

$$\theta = \arccos\left(\frac{\mathbf{r}_\mathcal{A} \cdot \mathbf{r}_{sol_\mathcal{A}}}{\|\mathbf{r}_\mathcal{A}\| \, \|\mathbf{r}_{sol_\mathcal{A}}\|} \right) \tag{28}$$

And thus, the incident solar radiation on the six sides of the CubeSat $n_{k_\mathcal{A}}$ is obtained by evaluating equation 22.

Next, a view factor based approach is used to predict the incident albedo radiation:[12,18]

$$q_{k,alb} = G_s V F_{k\to e} b_{alb} \Lambda_{alb} \tag{29}$$

, where $VF_{k\to e}$ denotes the view factor from each face (k=1..6) to Earth, which is that of an *arbitrarily oriented differential planar element to a sphere*.[18–20] It is evaluated based on figure 12:

$$\rho_k = \pi - \arccos\left(\frac{\mathbf{r}_\mathcal{A} \cdot \mathbf{n}_{k_\mathcal{A}}}{\|\mathbf{r}_\mathcal{A}\| \|\mathbf{n}_{k_\mathcal{A}}\|} \right) \tag{30}$$

The angle Φ is compared to ρ to determine whether or not the tangent to the surface passes through the sphere:

$$\Phi = \arcsin\left(\frac{1}{H} \right) \tag{31}$$

, where H is defined as the ratio between the magnitude of the CubeSat's position vector and Earth's radius. The virtual source of the albedo radiation is roughly 30km above Earth's surface, and is thus added to the radius:[17]

$$H = \frac{\|\mathbf{r}_\mathcal{A}\|}{(r_e + 30\,\mathrm{km})} \tag{32}$$

Three cases arise:

Case 1 - the tangent does not pass through the sphere if: $\rho_k + \Phi \leq \pi/2$

$$VF_{k\to e} = \frac{(\cos\rho_k)}{H^2} \tag{33}$$

Case 2 - the tangent passes through the sphere if: $\pi/2 - \Phi < \rho_k \leq \pi/2 + \Phi$

$$t_1 = H^2 \arcsin\left(\frac{\sqrt{H^2-1}}{H\sin(\rho_k)}\right) \tag{34a}$$

$$t_2 = \cos(\rho_k)\arccos\left(-\sqrt{H^2-1}\cot(\rho_k)\right) \tag{34b}$$

$$t_3 = \sqrt{(H^2-1)\left(1-H^2(\cos(\rho_k))\right)^2} \tag{34c}$$

$$VF_{k\to e} = \frac{1}{2} + \frac{1}{\pi H^2}(-t_1 + t_2 - t_3) \tag{34d}$$

Case 3 - the surface faces away from the sphere if: $\Phi + \pi/2 < \rho_k$

$$VF_{k\to e} = 0 \tag{35}$$

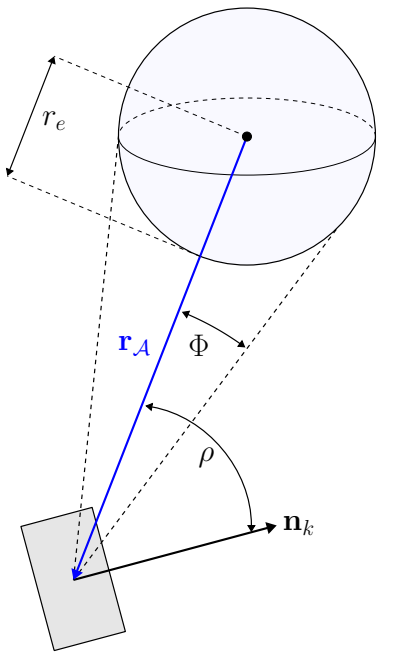

Figure 12: View factor from a differential plane to a sphere

Due to the large thermal inertia of the spacecraft with respect to occuring changes in the albedo factor, it is assumed constant with a value of $b_{alb} = 0.306$.[14,15] The function Λ_{alb} is introduced to reflect the fact that the satellite only receives albedo when above a part of Earth that is sunlit:[12,17]

$$\Lambda_{alb} = \begin{cases} \cos(\theta) & , 0 \leq \theta \leq \frac{\pi}{2} \\ 0 & , else \end{cases} \tag{36}$$

The incident Earth infrared radiation on the CubeSat is modeled by applying the view factor derived in the previous section and assumes Earth radiating uniformly in all directions according to the Stefan-Boltzmann law:[16]

$$q_{k,eir} = VF_{k\to e}\sigma T_e^4 \tag{37}$$

, where $\sigma = 5.670\,374 \times 10^{-8}\,\mathrm{Wm^{-2}K^{-4}}$ denotes the Stefan-Boltzmann constant and $T_e = 254.0\,\mathrm{K}$ the approximate black body temperature of Earth.[14] In the case of Earth-infrared however, the source is modeled directly from Earth's surface.

The total incident radiation on each face is the sum of the solar, albedo and Earth-infrared radiation respectively:

$$q_{k,tot} = q_{k,solar} + q_{k,albedo} + q_{k,eir} \tag{38}$$

The model is evaluated using *Matlab*, with figure 13 displaying the results of the AFWTR orbit at $\Gamma_0 = 0°$.

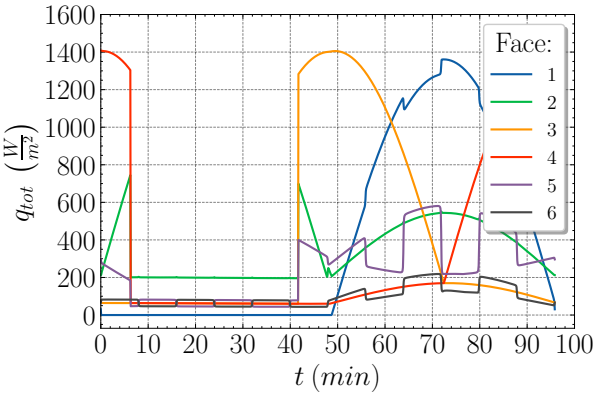

Figure 13: Total incident radiation of the AFWTR orbit for $\Gamma_0 = 0°$

A single, constant absorbtance (α) is assumed for radiation of all wavelengths, causing minor inaccuracies due to the difference in spectral composition of solar/albedo and earth infrared radiation:[4,15]

$$q_{k,abs} = \alpha_{sol}\left(q_{k,solar} + q_{k,alb} + q_{k,eir}\right) \tag{39}$$

, which is evaluated for each material/coating on each side of the CubeSat. The average incident radiation for each face ($k = 1..6$) over one orbit is used to derive initial temperatures in a steady-state

simulation:

$$\bar{q}_{k,solar} = \frac{1}{T}\int_0^T q_{k,solar}(t)\,\mathrm{d}t \tag{40a}$$

$$\bar{q}_{k,albedo} = \frac{1}{T}\int_0^T q_{k,albedo}(t)\,\mathrm{d}t \tag{40b}$$

$$\bar{q}_{k,eir} = \frac{1}{T}\int_0^T q_{k,eir}(t)\,\mathrm{d}t \tag{40c}$$

In identical fashion, the mean total absorbed radiation is:

$$\bar{q}_{k,abs} = \alpha_{sol}\left(\bar{q}_{k,solar} + \bar{q}_{k,albedo} + \bar{q}_{k,eir}\right) \tag{41}$$

Both dissipative radiation to space and internal radiation between components may be directly implemented into the *ANSYS* model and thus need not be modeled. Dissipation to space for each face k follows the Stefan-Boltzmann law:

$$q_{k\to\infty} = \sigma\epsilon\left(T_k^4 - T_\infty^4\right) \tag{42}$$

, where $\epsilon \in [0,1]$ denotes the surface's emittance, T_k the surface temperature, and T_∞ the ambient temperature. Radiation between bodies follows the same law and only introduces the extra view-factor between the respective bodies.

The beta angle (β) is often used to simplify the spacecraft thermal environment (figure 14).[21]

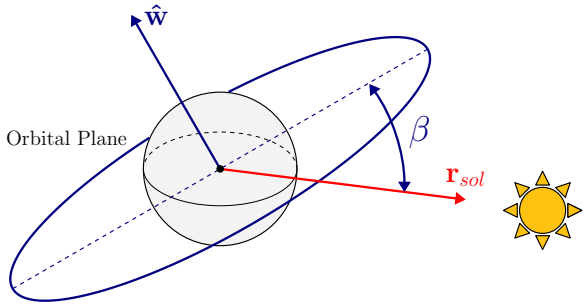

Figure 14: The beta angle

It is defined as the angle between the solar vector and its projection onto the orbital plane and may be calculated as follows:[16]

$$\begin{aligned}\beta = \arcsin\big[&\cos(\Gamma)\sin(\Omega)\sin(i)\\ &-\sin(\Gamma)\cos(\gamma_{ecl})\cos(\Omega)\sin(i)\\ &+\sin(\Gamma)\sin(\gamma_{ecl})\cos(i)\big]\end{aligned} \tag{43}$$

Its importance arises from two key influences the beta angle has on the thermal environment:[22] the variation of incident sunlight and albedo, as well as the variation of the amount of time spent in Earth's eclipse. With orbital perturbations (Ω) and the movement of the sun (Γ) being the major origin for those changes.[16]

Often, the beta angle is used in tabular or heavily simplified analytical approaches.[23] It is generally considered to be a valid tool and one may be confident that by analyzing multiple values of the beta angle, thermal load variations are accurately represented.[22]

Most eminently, NASA's technical standard for GSFC flight programs encourages environmental simulations to include steady-state conditions based on orbital averages.[24]

Because thermal load variations are properly represented when analyzing multiple values of the beta angle, it serves as the main measure of variation for an orbit. In common literature two extreme cases of beta are often analyzed: first, the coldest case, in which the satellite spends most time in Earth's shadow, indicated by a beta of around 0°. Second, the hottest case, where the satellite spends no time at all in Earth's shadow, which is usually for beta angles between 75° and 90°. Table 2 shows different beta angles for the AFWTR orbit.

Table 2: Beta angles for different values of Γ

Orbit	$\Omega(^\circ)$	$i(^\circ)$	$\Gamma(^\circ)$	$\beta(^\circ)$
AFWTR	9.8	97.58	0	9.71
			90	-71.56
			180	-9.71
			270	71.56

The AFWTR orbit will later be evaluated using $\Gamma_0 = 0^\circ$ as the cold case and $\Gamma_0 = 90^\circ$ as the hot case.

MATERIAL PROPERTIES

A total of eleven materials are applied in the model, selected in compliance with NASAs *Standard for Materials and Processes Requirements for Spacecraft* and later assigned to all parts in the *ANSYS* model.[25] Collected are the material's density, specific heat capacity, and thermal conductivity. All selected materials are gathered in table 3.

Data for both the specific heat and thermal conductivity are shown in table 4. Due to the high temperature gradients a satellite can experience between the sun facing and sun averting side, temperature dependent data was collected. Additionally, thermal conductivity is assumed to be isotropic for all materials.

Table 3: Material selection

Material	Details	Density (kg/m^3)
316SS[26]	X5CrNiMo17-12-2	7916.45
6061Al[26]	AMS4026 T6	2712.63
Brass[27]	CuZn28Sn1As	8560.00
Copper[27]	Cu	8960.00
Silicon[27]	Monocrystalline	2330.00
BK7[28]	Borosilicate Glass	2504.00
Silicone[29]	Polysiloxane	970.00
PEEK[29]	Polyether-ether-ketone	1264.00
E-Glass[30]	BK7 epoxy composite	1750.00
Epoxy Resin[31]	Araldite MY 740	1210.00
Lithium-Ion[32]	Sony US18650GR Cell	2560.00

Table 4: Thermal properties of selected materials

(a) Specific heat

	c_p $(J/(kg\ K))$				
Material	$-100°C$	$0°C$	$100°C$	$200°C$	$300°C$
316SS[26]	377	440	500	523	544
6061Al[26]	670	837	942	1005	1047
Brass[27]	-	376	-	-	399
Copper[33]	338	379	399	408	417
Silicon[34]	660	691	770	825	848
BK7[28]	640	740	840	940	1040
	$-20°C$	$0°C$	$25°C$	-	-
Silicone[29]	1439	1450	1460	-	-
	$25°C$	$77°C$	$127°C$	$177°C$	$227°C$
PEEK[29]	1250	1270	1679	1835	1939
	$-100°C$	$-30°C$	$89°C$	$105°C$	$200°C$
E-Glass[35]	558	748	1070	1243	1352
	$-123°C$	$-73°C$	$-23°C$	$27°C$	$127°C$
Epoxy Resin[36]	2220	2030	1840	1650	1270
	-	-	$25°C$	-	-
Lithium-Ion[32]	-	-	612	-	-

(b) Thermal conductivity

	k $(W/(m\ K))$				
Material	$-100°C$	$0°C$	$100°C$	$200°C$	$300°C$
316SS[26]	13	15.6	16.3	17.4	18.9
6061Al[26]	125	147	162.6	173	182
Brass[27]	99	110	120	136	152
Copper[37]	428	401	393	389	384
Silicon[38]	325	176	119	87	68
BK7[28]	0.78	1.04	1.11	1.19	1.43
	$-40°C$	$0°C$	$40°C$	$80°C$	$120°C$
Silicone[39]	0.26	0.24	0.22	0.2	0.18
	-	-	$25°C$	-	-
PEEK[29]	-	-	0.25	-	-
	$-100°C$	$-30°C$	$89°C$	$105°C$	$200°C$
E-Glass[35]	0.366	0.369	0.352	0.338	0.321
	$-123°C$	$-73°C$	$-23°C$	$27°C$	$127°C$
Epoxy Resin[31]	0.18	0.21	0.23	0.25	0.26
	-	-	$25°C$	-	-
Lithium-Ion[32]	-	-	1.845	-	-

As for the optical material properties, both absorbtance and emittance for the different materials and finishes are gathered. By virtue of their extremely variable nature, the limitation of *ANSYS* to diffusive-gray-opaque bodies, and considering that within this initial analysis many surface/material finishes are not yet well defined, constant values are hereby assumed.[40] Most importantly, absorbtances values are gathered for the *solar* spectrum, while emittance values are gathered for the *infrared* (around room-temperature) spectrum. Two main resources were applied to gather the data: the NASA Goddard Space Flight Center provides a comprehensive list of properties in both spectrums for common spacecraft components and many coatings.[41] In addition, if necessary, accompanying data was gathered from the VDI Heat-Atlas.[27] Results are listed in table 5.

Table 5: Optical material properties

Material	Description	α_{sol}	ϵ_{IR}
316SS	Machined	0.47	0.14
6061Al	Plain anodized	0.3	0.095
6061Al	Black anodized	0.86	0.86
Brass	Non-oxidized	0.65	0.03
Copper	Polished	0.32	0.03
Silicon	Oxidized	0.8	0.8
BK7	-	0.05	0.9
Silicone	White color	0.4	0.9
PEEK	White color	0.4	0.95
E-Glass	Estimate	0.1	0.92
Epoxy Resin	Brown color	0.6	0.85
Solar Panels	-	0.8	0.8

FINITE ELEMENT MODEL

The next major step in the thermal modeling process is to build and prepare the Finite Element Model. In essence, the goal is to obtain a full model up to the point where only orbit specific loads need to be applied and the model may be simulated with them.

First, the model geometry is simplified, shortening simulation times while maintaining a level of detail that still accurately depicts the propulsion system. The following key principles were applied:

Preserve functionality - The simplification may not infringe the general capability of the CubeSat to perform its primary mission. As an example, solar panels may not be removed as the satellite can't operate without power.

Preserve physical properties - Key properties to the thermal analysis, such as mass and subsequently thermal mass shall be preserved as best as possible.

Remove unnecessary details - Any detail that is either cosmetic or serves no function from a thermal viewpoint is removed, e.g. chamfers.

Maintain FEMTA detail - The level of detail in the FEMTA system itself shall be maintained.

The results of this process are shown in figure 15. As one may see, the general structure of the satellite remains the same, while many details were removed.

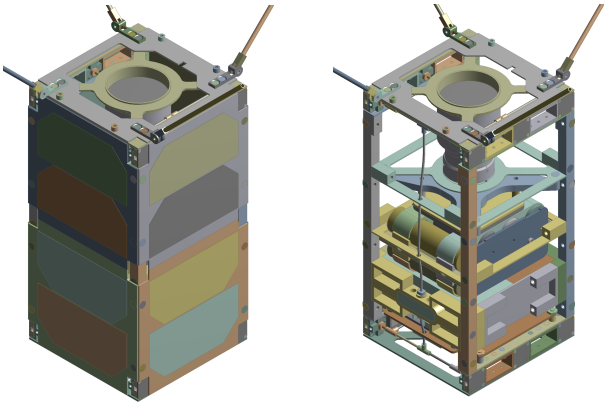

(a) Initial

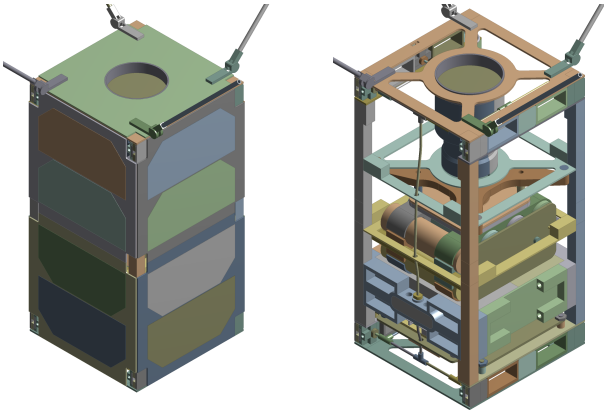

(b) Simplified

Figure 15: Comparison of the initial and simplified geometry in ANSYS Design Modeler

Next all boundary conditions and loads are applied to the Finite Element Model. Namely conduction between parts, internal heat production of electrical components, and radiation.

Conduction includes both the internal heat transmitted within a part, and the heat transmitted between parts in contact. Internal heat transmission within a single part is directly evaluated by *ANSYS* based on the thermal conductivity specified for the material. Regarding contact conductance however, even when disregarding surface finish, surface roughness, contact pressure, and all other influences,[42] a total of 55 possible pairings arise when using only 11 principle materials. Because many of these parameters, such as the surface roughness, are not yet well defined for the model at this stage, as well as the limited data available, contact conductance is assumed to be perfect between all bodies.

In this particular model, a total of over 2500 contacts are implemented. All of these contacts were checked for errors by hand. An example is given in figure 16: the PCB, colored in blue, is in perfect contact with the red area of the heat sink.

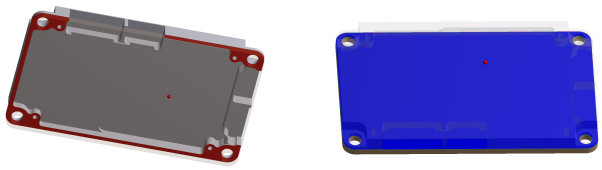

(a) AX100 heat sink **(b) AX100 PCB**

Figure 16: Example contact pair definition in *ANSYS* for the AX100

The power consumption of many of the electrical components is implemented as internal heat generation. For each component, an operating mode along with the produced heat is estimated based on information gathered from each respective datasheet.

Table 6: Internal heat production[43–50]

Part	Operating Mode	Power (W)
A3200	base speed	0.170
DMC-3	base speed	0.814
AX100	10% on-time	0.282
ANT430	-	-
BPX	Heaters on 5% of time	0.407
P110	-	-
GPS	50% power	0.690
C1U	1 picture every 5 minutes	0.401

Displayed in table 6 are the assumed operating state alongside the resulting power production for all parts.

Three types of radiative heat transfer are modeled: the incident radiation, dissipative radiation to space, and surface-to-surface radiation between bodies. For all of these the following key assumptions uphold:[51]

Opaque surfaces - no radiative heat transfer occurs within bodies themselves. Their transmittance is zero.

Transparent space - space as a medium is entirely transparent.

Constant emittance and absorbtance - both the absorbtance and emittance of any body or surface remain constant.

The incident radiation is modeled as a surface heat flux boundary condition for both the steady state and transient simulations.

As depicted in figure 17, it is assigned the following way: first, the radiation is calculated for all six faces using the previously derived model. Then, it is scaled by the respective solar absorbtance (α_{sol}) of each material. Lastly, faces with the same absorbtance are grouped together in the FE model and all heat fluxes are applied. The workflow is outlined for face number three, with a total of four different materials/finishes.

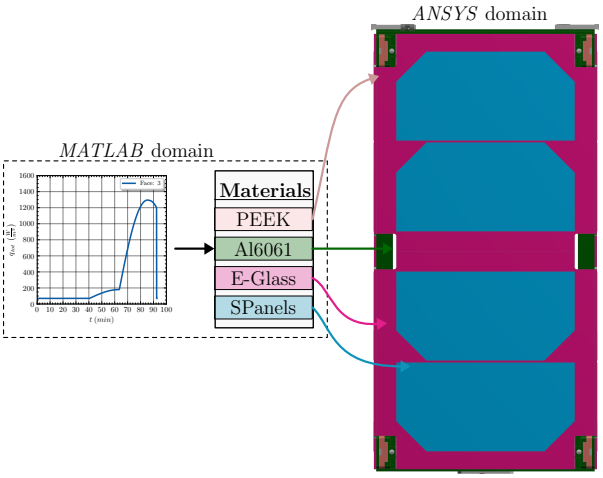

Figure 17: Workflow: assigning the incident radiation to face three

Dissipative radiation to space is implemented in similar fashion, as shown in figure 18.

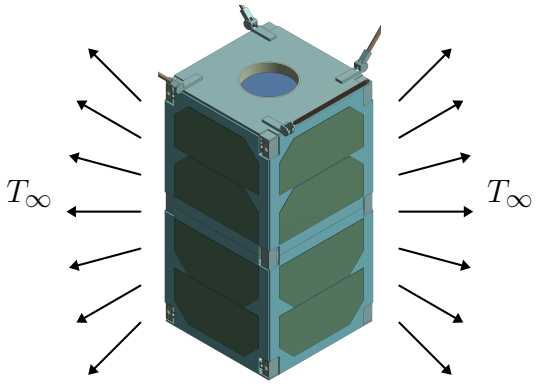

Figure 18: Dissipative radiation to space in *ANSYS*. Each color denotes a different surface emmitance.

It follows the Stefan-Boltzmann law and may be directly implemented as a radiation boundary condition into *ANSYS* by specifying infrared emittance (ϵ_{IR}) along with ambient temperature (T_∞), which is set to $-270\,^\circ$C.

Surface-to-surface radiation may also be implemented directly into *ANSYS* as a radiation boundary condition, but is limited to gray-diffuse bodies. Figure 19 shows the two major enclosures where internal radiation is exchanged, each highlighted in red. The importance for surface-to-surface radiation in evaluating the FEMTA propulsion system becomes clear, as the tubing is barely in contact with other components and its main mode of heat transfer is thus radiation.

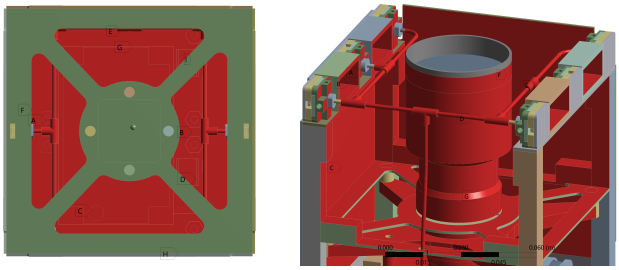

(a) First enclosure **(b) Second enclosure**

Figure 19: Surface-to-surface radiation

With all boundary conditions and loads applied, the next step in the thermal modeling process is to mesh the geometry. It is crucial to achieve the best quality mesh possible for a given maximum simulation time. To achieve this, one has the option to vary element size, type, and shape. The following considerations uphold:[52]

Sizing - the size of the element should be chosen in accordance with the necessary level of resolution. Local refinement or coarsening is used to achieve desired accuracy in certain areas.

Element type - for heat transfer problems, first order elements are often sufficient.

Element shape - quadrilateral or hexahedral elements shall be used whenever possible.

ANSYS Mechanical provides both the possibility to auto-generate a mesh with general sizing criteria, as well as to locate and display lower quality elements. These functions in addition to the outlined principles form the general approach to the meshing process.

Using the AFWTR orbit with $\Gamma_0 = 0\,^\circ$ as input, a total of 13 steady-state simulations with identical boundary conditions were run and the total number of DOF was varied from approximately 75 000 to 550 000. As numerous parts of the model have boundary conditions applied to them, refinement was conducted globally and for all parts within each

consecutive iteration. Temperatures were evaluated at numerous bodies, surfaces, and points crucial to the model, with focus on the propulsion system. Additional measures on other parts were gathered in identical fashion, but will not be listed. Figure 20 shows the temperature behavior for various entities of the propellant tank.

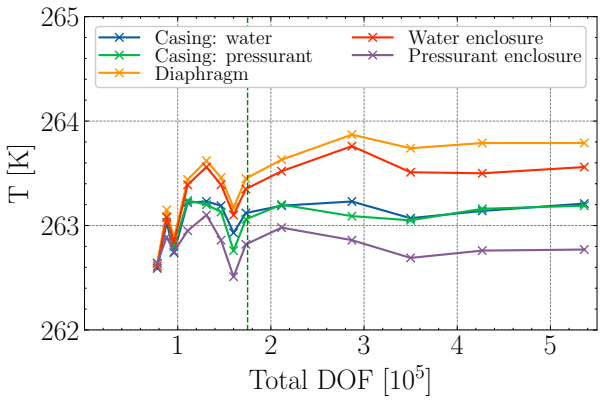

Figure 20: Mesh convergence evaluated for the FEMTA propellant tank

Initially, temperatures display a very volatile behavior from 75 000 to about 150 000 DOF. From 175 000 DOF on, indicated by the dashed vertical line, an acceptable converging behavior arises with temperature fluctuations within ±0.5 K.

Similar behavior is observed for the tubing. Here, the average surface temperatures of the inlets for all twelve FEMTA chips were gathered. Results are shown in figure 21.

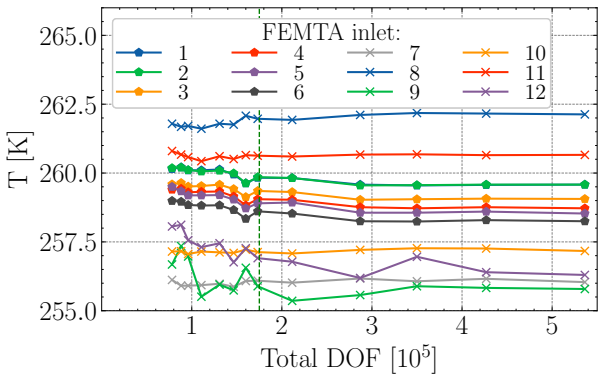

Figure 21: Mesh convergence evaluated for the propellant tank

Again, after a settling period between 75 000 and 175 000 DOF, temperatures begin to converge and most show variations for each consecutive iteration below 0.5 K.

Estimated from these results, a general mesh size of 200 000 nodes is deemed sufficient to accurately evaluate the temperature behavior of the FEMTA propulsion system within this initial demonstration of the thermal assessment architecture. The final mesh is shown in figure 22.

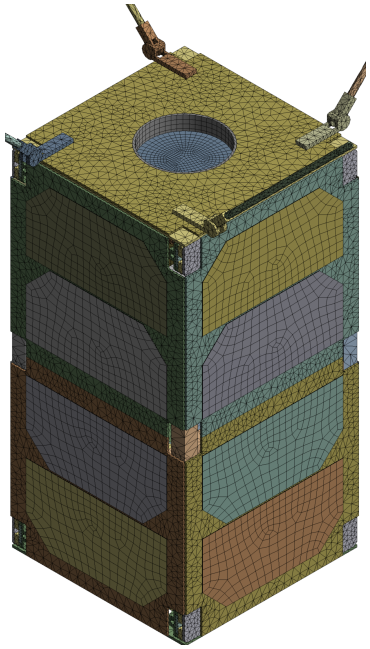

Figure 22: The final mesh

It consists of linear elements with about 190 000 nodes and 350 000 elements. Based on the convergence analysis, it is to assume that the confidence for the propulsion system component temperature values are well within ±1 K.

SOLUTION PROCEDURE

With all precursor steps done and the FE model being finished, one may then choose an orbit and simulate the model. In order to demonstrate the power of the outlined workflow, and to gain an initial assessment of FEMTA behavior, the AFWTR orbit is evaluated at $\Gamma_0 = 0\,^\circ$ with $\beta_0 = 9.71\,^\circ$, and at $\Gamma_0 = 90\,^\circ$ with $\beta_0 = 71.56\,^\circ$.

The results from these two simulations are then briefly evaluated and discussed. The predicted incident radiation is shown in figure 23.

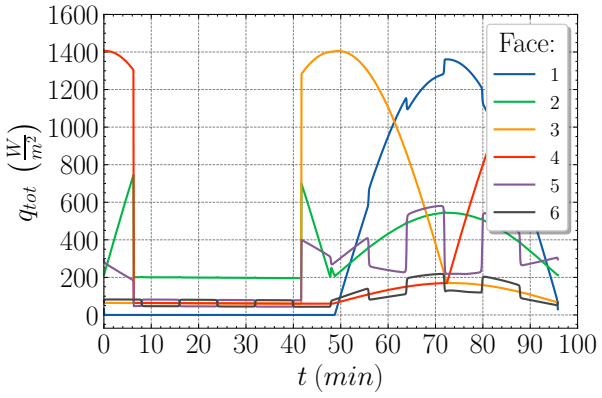

(a) $\Gamma_0 = 0\,^\circ$, $\beta_0 = 9.71\,^\circ$

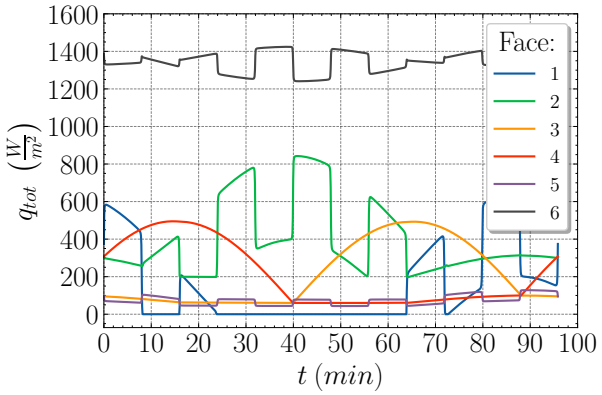

(b) $\Gamma_0 = 90\,^\circ$, $\beta_0 = 71.56\,^\circ$

Figure 23: Inputs to the two simulations run for the AFWTR orbit

The average values for the incident radiation are shown in table 7. Incidentally, Wertz et al. have derived tabular values for a nadir pointing CubeSat based on the beta angle as well. When comparing their values to the ones derived with the proposed model for a similar orbit, differences are within $\pm 10\,\%$, further validating the radiation model.[4]

Finally, to evaluate the model steady-state simulations are run using the average values, followed by the transient simulation over one orbit.

Table 7: Average incident radiation in $\mathrm{W/m^2}$ for the AFWTR orbit

Γ_0	β_0	k	$\bar{q}_{k,solar}$	$\bar{q}_{k,albedo}$	$\bar{q}_{k,eir}$	$\bar{q}_{k,abs}$
0°	9.71°	1	420.45	0	0	420.45
		2	35.12	109.78	198.45	343.35
		3	304.90	34.27	61.94	401.11
		4	293.00	34.27	61.94	389.21
		5	142.99	34.76	62.72	240.47
		6	0.17	34.75	62.72	97.54
90°	71.56°	1	152.67	0	0	152.67
		2	154.83	35.31	198.45	388.59
		3	137.62	11.17	61.94	210.73
		4	136.37	11.17	61.94	209.48
		5	0	11.31	62.72	74.03
		6	1272.11	11.30	62.72	1346.13

RESULTS

After successfully running the simulations, results are gathered. As in this case the model is highly detailed, the analysis is restricted to broader conclusions that may be drawn for the FEMTA propulsion system.

Subsequently, in line with the model requirements, results for the propellant tank are hereby displayed, along with general points of interest. Total simulation time for both cases was about 22 h (Windows10, Intel(R) Xeon(R) E3-1270 v5 @3.60 GHz, 64GB DDR3) and a total of 200 time steps, each with a length of about 28.7 s, were evaluated.

In the cold case, the CubeSat is exposed to strong temperature variations. With a total average temperature between $-35\,^\circ$C and $0\,^\circ$C, the impact of Earth's eclipse becomes apparent. Minimum, maximum, and average temperature of the CubeSat are displayed in figure 24.

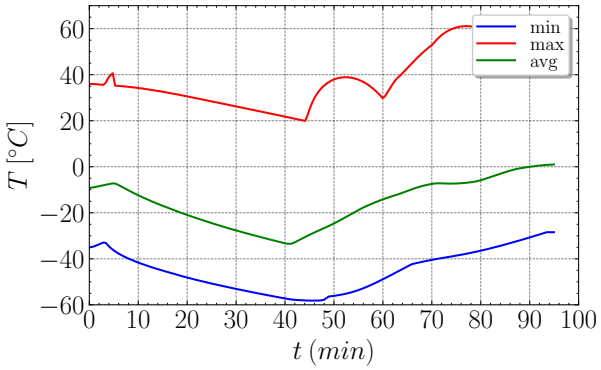

Figure 24: Cold case temperature variations for the whole CubeSat

The average initial temperature after the steady-state simulation is about $-5\,^\circ$C. Quickly, the CubeSat enters Earth's eclipse and the average tempera-

ture drops to almost −40 °C. At about 42 min, the arising incident solar radiation starts to heat up the CubeSat to an average of about 0 °C. The same behavior is observable for the minimum and maximum temperatures. Multiple snapshots of the temperature variation for the CubeSat over the orbit are shown in figure 25.

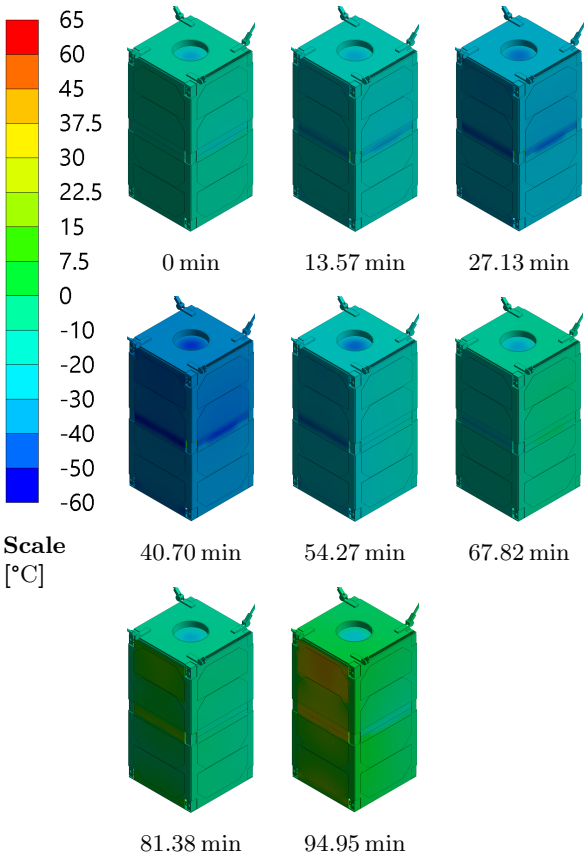

Figure 25: Isometric view of the temperature change for the cold case

The CubeSat's rapid cooldown while in Earth's eclipse is clearly visible, with temperatures rising again only after solar radiation begins to fall onto the CubeSat. In addition, the large difference between incident radiation for different surfaces becomes apparent at the end of the orbit, with some faces heating up to almost 40 °C, while other remain in the negatives.

An argument in favor of the FEMTA requirements not being met may be made just by judging this behavior. It is unlikely that the water and pressurant will remain above the required 15 °C, when average temperatures never exceed 0 °C. It is already the first indicator that a design change and/or thermal management system is necessary.

The propellant tank is evaluated at multiple bodies, namely the water casing, diaphragm, and pressurant casing. Figure 26 illustrates where exactly the body temperatures were evaluated. Displayed are the temperature distributions at $t = 94.95$ min, the end of the orbit, for all three bodies.

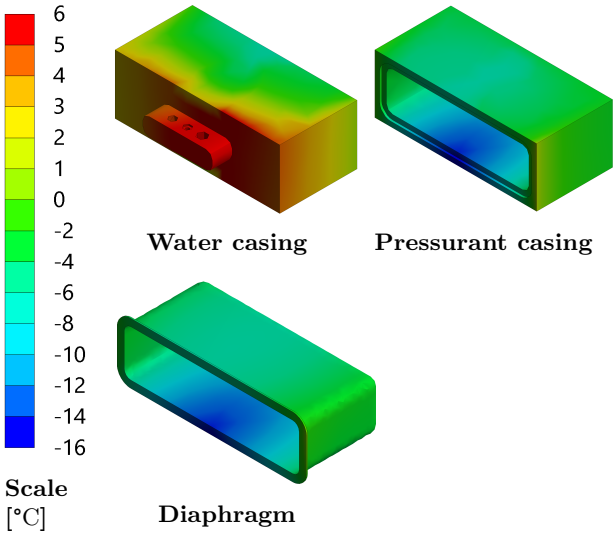

Figure 26: Cold case end temperature distributions for the three main tank parts

For all three of them, average initial temperatures range from about −15 °C to slightly above 0 °C at some points. However, over the course of the orbit temperatures drop much further, as may be seen in figure 27.

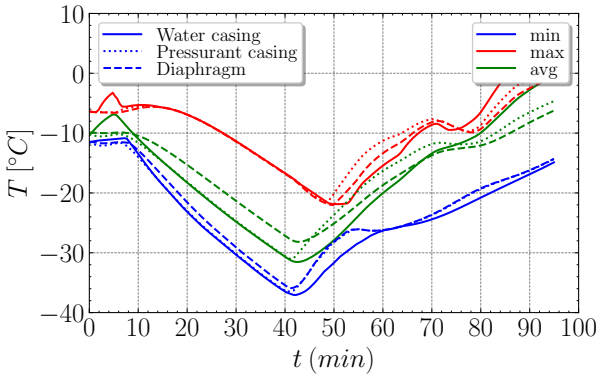

Figure 27: Cold case body temperature histories for the three main tank parts

Temperature variations are much less severe for the hot case, as the CubeSat constantly receives solar radiation. Subsequently, temperatures in general are much higher, as shown in figure 28.

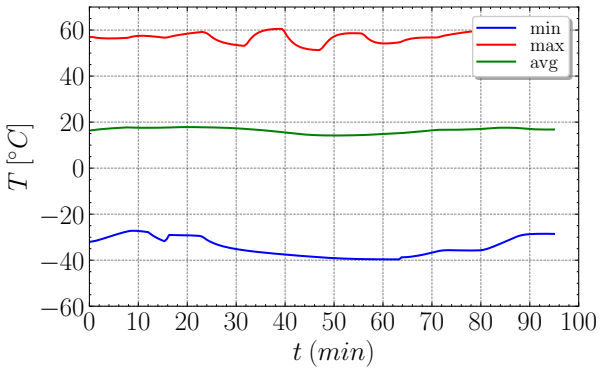

Figure 28: Hot case temperature variations for the whole CubeSat

Multiple snapshots of the CubeSat over the span of its orbit are shown in figure 29.

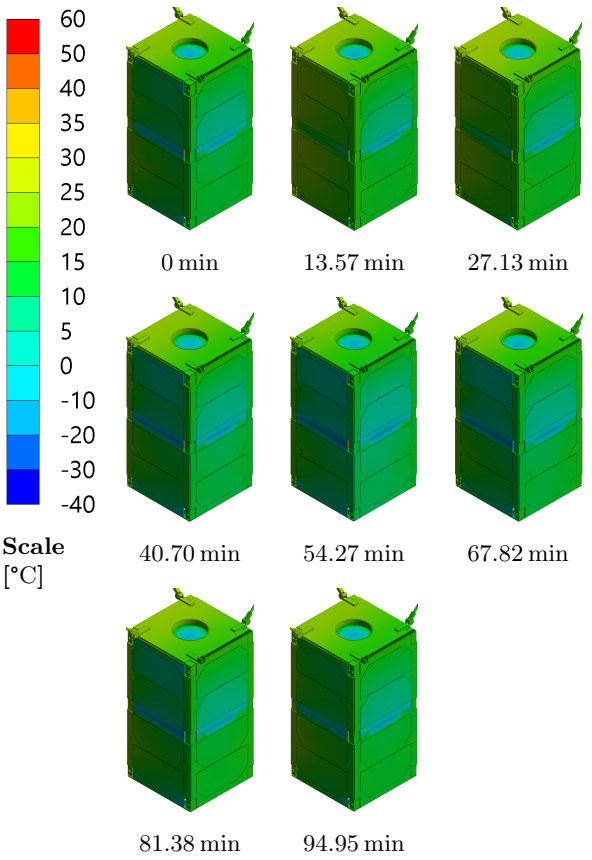

Figure 29: Isometric view of the temperature change for the hot case

The average initial temperature after the steady-state simulation is about 15 °C and remains almost constant over the course of the orbit. Similarly, minimum and maximum temperatures within the CubeSat show little variation as well and hover at around −30 °C for the minimum, and 60 °C for the maximum temperature.

Temperature variations are barely visible and surface temperatures are almost constant. When taking a closer look, it is observable that the left most face (face 4) initially heats up due to the radiation falling onto it and begins to cool back down at about 40 minutes once it rotates away from the sun. This behavior is expected when considering the radiation input as shown in figure 23.

Contrary to the cold case, the average temperature of over 15 °C and its relatively low volatility are a first indicator that the model requirements may be met.

The same may be observed for the water casing, diaphragm, and pressurant casing, who's body temperatures are displayed in figure 30.

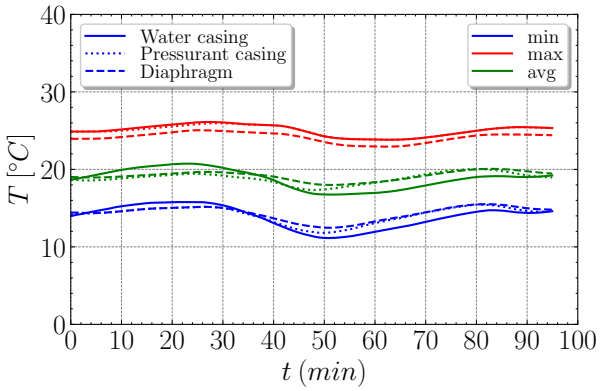

Figure 30: Hot case body temperature histories for the three main tank parts

For the propellant tank, average temperature remains relatively constant at around 20 °C and fluctuates by a couple degrees at most. Even the minimum temperatures within the tank persist at around 15 °C and never drop below 10 °C. Maximum temperatures stay well below 30 °C throughout the entire orbit.

CONCLUSIONS

The objective of this work was to evaluate the transient-thermal response of a preliminary FEMTA micropropulsion system design operating on a CubeSat in Low Earth Orbit. To achieve this, a generalizable analysis process specifically for Low Earth Orbit CubeSat missions was developed. A single iteration

of this process was performed, both to demonstrate how each consecutive step itself is carried out, as well as to gain an initial set of results.

This included a complete virtual mission design for an entirely operational CubeSat model, the derivation of a full orbit, attitude and radiation model, and the implementation of a finite element model. The FE model was then simulated in two extreme thermal environments, the effectiveness of the FEMTA propulsion system evaluated, and overall points of improvement outlined.

It has been shown that the proposed analysis process is able to provide detailed and precise insights to the thermal response of CubeSats. Furthermore, the resulting temperature predictions strongly suggest the necessity of a thermal management system for the FEMTA propulsion system. Temperatures within the propulsion system did not exceed the upper temperature requirement of 30 °C for either scenario. However, in both the hot and cold cases, propulsion system temperatures dropped well below 15 °C. Total power loss through the propellant tank walls was less than 2 W for the hot case and less than 0.5 W for the cold case. A significant portion of this energy is lost through the bottom face of the propellant tank which is exposed to the ambient space environment. Simply enclosing the satellite internal volume should help mitigate this heat loss. Regardless, it is still clear that internal heat sources will need to be integrated into the propellant tank to satisfy the minimum temperature requirement. Additionally, propellant feed tubing should be insulated to prevent cooling while propellant is stagnant in the tubes for extended duration. Further analysis should be performed with FEMTA node faces exposed to the ambient environment in order to determine whether this configuration would present a risk of misfiring or ice formation.

The primary limitation of this work is the absence of adequate modeling of the water and pressurant fluid within the system. Solutions to this problem, alongside other points of improvement, have been discussed and will be vital to the derivation of a final thermal management system. In conclusion, this work serves as the initial spark to the long iterative process that will be managed by future Purdue students to derive a suitable thermal management system as part of the UNP, and may be used as a general guide for other CubeSat designers.

References

[1] Steven Pugia, Anthony Cofer, and Alina Alexeenko. Characterization of film-evaporating microcapillaries for water-based microthrusters. *Acta Astronautica*, September 2020.

[2] Anthony George Cofer. *Film evaporation MEMS thruster array for micropropulsion.* PhD Thesis, Purdue University, West-Lafayette, Indiana, 2015.

[3] Steven M. Pugia. Reliability Investigation and Design Improvement of FEMTA Microthruster. Master's thesis, Purdue University Graduate School, October 2021.

[4] James Richard Wertz, David F. Everett, and Jeffery John Puschell. *Space mission engineering: the new SMAD.* Number v. 28 in Space technology library. Microcosm Press : Sold and distributed worldwide by Microcosm Astronautics Books, Hawthorne, CA, 2011. OCLC: ocn747731146.

[5] Thyrso Villela, Cesar A. Costa, Alessandra M. Brandão, Fernando T. Bueno, and Rodrigo Leonardi. Towards the Thousandth CubeSat: A Statistical Overview. *International Journal of Aerospace Engineering*, 2019:1–13, January 2019.

[6] Erik Kulu. Nanosats Database. est. 2014.

[7] Gunter D. Krebs. Gunter's Space Page - Information on spaceflight, launch vehicles and satellites. est. 1996.

[8] N2YO.com - real time satellite tracking. est. 2008.

[9] T.S. Kelso. CELESTRAK. est. 1985.

[10] A. E. Roy. *Orbital motion.* Institute of Physics Pub, Bristol, England ; Philadelphia, 4th ed edition, 2005.

[11] Oliver Montenbruck and Eberhard Gill. *Satellite Orbits.* Springer Berlin, Heidelberg, Berlin, Heidelberg, 2000.

[12] Edemar Morsch Filho, Laio Oriel Seman, Cezar Antônio Rigo, Vicente de Paulo Nicolau, Raúl García Ovejero, and Valderi Reis Quietinho Leithardt. Irradiation Flux Modelling for Thermal–Electrical Simulation of CubeSats: Orbit, Attitude and Radiation Integration. *Energies*, 13(24):6691, December 2020.

[13] Tilo Arens, Frank Hettlich, Christian Karpfinger, Ulrich Kockelkorn, Klaus Lichtenegger, and Hellmuth Stachel. *Mathematik*. Lehrbuch. Springer Spektrum, Berlin [Heidelberg], 4th revision edition, 2018.

[14] David R. Dr. Williams. Earth Fact Sheet. Last Updated 12/2021.

[15] Peter Fortescue. *Spacecraft Systems Engineering*. Wiley, Chicester, 4th ed. edition, 2011.

[16] Gary Eugene Musgrave, Axel M. Larsen, Tommaso Sgobba, and International Association for the Advancement of Space Safety, editors. *Safety design for space systems*. Butterworth-Heinemann, Burlington, MA ; Oxford, 2009. OCLC: ocn260207481.

[17] B.J. Anderson, C.G. Justus, and G.W. Batts. Guidelines for the Selection of Near Earth Thermal Environment Parameters for Spacecraft Design. *NASA Technical Memorandum*, 211221, 2001.

[18] John Anger Richmond. *Adaptive thermal modeling architecture for small satellite applications*. PhD Thesis, Massachusetts Institute of Technology, Cambridge, Massachusetts, 2010.

[19] John R. Howell, M. Pinar Menguc, and Robert Siegel. *Thermal Radiation Heat Transfer*. CRC Press, September 2015.

[20] John R. Howell. A Catalog of Radiation Heat Transfer Configuration Factors, 2020.

[21] Bruce R. Barkstrom. The Earth Radiation Budget Experiment (ERBE). *Bulletin of the American Meteorological Society*, 65(11):1170–1185, November 1984.

[22] David G. Gilmore, editor. *Spacecraft thermal control handbook*. Aerospace Press, El Segundo, Calif, 2nd ed edition, 2002.

[23] S.L. Rickman. A Simplified, Closed-Form Method for Screening Spacecraft Orbital Heating Variations. December 2002.

[24] Michael Viens. General Environmental Verification Standard (GEVS) for GSFC Flight Programs and Projects. Technical Report GSFC-STD-7000B, NASA, April 2021.

[25] Ralph R. Jr. Roe. Standard Materials and Processes Requirements for Spacecraft. Technical Report NASA-STD-6061C, NASA, September 2021.

[26] *MMPDS-16*. Metallic Materials Properties Development and Standardization. Battelle Memorial Institute, October 2021.

[27] VDI e. V., editor. *VDI Heat Atlas*. Springer Berlin Heidelberg, Berlin, Heidelberg, 2010.

[28] M. J. Assael, S. Botsios, K. Gialou, and I. N. Metaxa. Thermal Conductivity of Polymethyl Methacrylate (PMMA) and Borosilicate Crown Glass BK7. *International Journal of Thermophysics*, 26(5):1595–1605, September 2005.

[29] James E. Mark. *Polymer data handbook*. Oxford University Press, 2nd ed edition, November 2009.

[30] Carl Zweben. Composite Materials. In *Mechanical Engineers' Handbook*, pages 1–37. John Wiley & Sons, Inc., Hoboken, NJ, USA, February 2015.

[31] K W Garrett and H M Rosenberg. The thermal conductivity of epoxy-resin / powder composite materials. *Journal of Physics D: Applied Physics*, 7(9):1247–1258, June 1974.

[32] Hossein Maleki, Said Al Hallaj, J. Robert Selman, Ralph B. Dinwiddie, and H. Wang. Thermal Properties of Lithium-Ion Battery and Components. *Journal of The Electrochemical Society*, 146(3):947–954, March 1999.

[33] Douglas L Martin. THE SPECIFIC HEAT OF COPPER FROM 20° TO 300 deg; K. *Canadian Journal of Physics*, 38:17–24, 1960.

[34] H. R. Shanks, P. D. Maycock, P. H. Sidles, and G. C. Danielson. Thermal Conductivity of Silicon from 300 to 1400 K. *Physical Review*, 130(5):1743–1748, June 1963. Publisher: American Physical Society.

[35] Georgios Kalogiannakis, Danny Van Hemelrijck, and Guy Van Assche. Measurements of Thermal Properties of Carbon/Epoxy and Glass/Epoxy using Modulated Temperature Differential Scanning Calorimetry. *Journal of Composite Materials*, 38(2):163–175, January 2004.

[36] Andrew A. Johnston. *An integrated model of the development of process-induced deformation in autoclave processing of composite structures*. PhD Thesis, University of British Columbia, 1997.

[37] RW Powell, Cho Yen Ho, and Peter Edward Liley. *Thermal conductivity of selected materials*, volume 8. US Department of Commerce, National Bureau of Standards Washington, DC, 1966.

[38] C. J. Glassbrenner and Glen A. Slack. Thermal Conductivity of Silicon and Germanium from 3 K to the Melting Point. *Physical Review*, 134(4A):A1058–A1069, May 1964. Publisher: American Physical Society.

[39] Akira Sugawara and Ichiro Takahashi. Thermal Conductivity of Polysiloxane in Intermediate Temperature Range. In P. G. Klemens and T. K. Chu, editors, *Thermal Conductivity 14*, pages 299–302. Springer US, Boston, MA, 1976.

[40] M. F. Modest. *Radiative heat transfer*. Academic Press, New York, 3rd edition, 2013. OCLC: ocn813855549.

[41] J. H. Henninger. Solar absorptance and thermal emittance of some common spacecraft thermal-control coatings, April 1984. NTRS Author Affiliations: NASA Goddard Space Flight Center NTRS Report/Patent Number: REPT-84F0248 NTRS Document ID: 19840015630 NTRS Research Center: Legacy CDMS (CDMS).

[42] Dieter Meschede. *Gerthsen Physik*. Springer-Lehrbuch. Springer Berlin Heidelberg, Berlin, Heidelberg, 2015.

[43] GomSpace. *NanoMind A3200 Datasheet*, 2021. Rev. 1.17.

[44] GomSpace. *NanoDock DMC-3 Datasheet*, 2021. Rev. 1.12.

[45] GomSpace. *NanoCom AX100 Datasheet*, 2019. Rev. 3.7.

[46] GomSpace. *NanoCom ANT430 Datasheet*, 2020. Rev. 4.1.

[47] GomSpace. *NanoPower BPX Datasheet*, 2019. Rev. 2.0.

[48] GomSpace. *NanoPower P110 Datasheet*, 2018. Rev. 2.10.

[49] GomSpace. *NanoSense GPS Kit Datasheet*, 2019. Rev. 2.3.

[50] GomSpace. *NanoCam C1U Datasheet*, 2018. Rev. 1.8.

[51] William Alan Gray and Rudolph Muller. *Engineering calculations in radiative heat transfer*. Number v. 13 in International series on materials science and technology. Pergamon Press, Oxford New York, 1st ed. edition, 1974.

[52] Klaus-Jürgen Bathe. *Finite Element Procedures*. Prentice Hall, 1996.